

Matter effects on flavor transitions of high-energy astrophysical neutrinos based on different decoherence schemes

Ding-Hui Xu^{1,*} and Shu-Jun Rong^{1,†}

¹*College of Science, Guilin University of Technology, Guilin, Guangxi 541004, China*

The progress of neutrino astronomy makes the precise measurement of the flavor ratio of high energy astronomical neutrinos (HANs) possible in the near future. Then matter effects and new physics effects on the flavor transition of HANs could be tested by the next-generation neutrino telescopes. In this paper we study matter effects in gas around the sources of HANs. The matter effects are dependent on both the decoherence schemes and the sources of neutrinos. We examine the predictions on the flavor ratio at Earth for typical sources with five decoherence schemes. For the adiabatic schemes, the matter effect is notable and may be identified in the special range of the electron density, irrespective of the production sources of HANs. Hence, the precise measurement of the flavor ratio would provide constrains on the propagation schemes and the matter parameter.

arXiv:2205.03164v3 [hep-ph] 30 Nov 2022

* 3036602895@qq.com

† rongshj@glut.edu.cn

I. INTRODUCTION

In the recent decade, many high-energy astrophysical neutrinos (HANs) events in the TeV - PeV energy range have been observed by the IceCube observatory[1–5]. The energy spectrum, flavor ratio, and sky distribution of HANs are analysed[6–10]. With the help of the synergetic observation of electromagnetic wave messengers, the promising sources of HANs are indicated[11–14]. Although considerable progress has been made in neutrino astronomy, there are several important problems to be solved: The uncertainty of flavor ratio measured at Earth is large[15, 16]; No source of HANs is identified above the 5σ discovery threshold; How to explain the multi-messenger emission from the blazar TXS0506+056 is challenging[17–19]; The production mechanism of HANs is unclear. Among these problems, the first one would be overcome with the operations of the next-generation neutrino telescopes[20–24] in the next two decades. Furthermore, since the energy spectrum and the flavor ratio of HANS at the source are determined by the production mechanism, the progress of the first one would also provide clues for the last one.

As is known, the flavor ratio at the source is inferred from that at Earth and the flavor transition probability of the HANs. Under the assumption that the leptonic mixing matrix at the source and that in the propagation path are the same as the one in vacuum, the so-called standard flavor transition matrix (FTM) is obtained after the decoherence of neutrinos, i.e.,

$$\overline{P}_{\alpha\beta}^s = \sum_i |U_{\alpha i}|^2 |U_{\beta i}|^2, \quad (1)$$

where U is the leptonic mixing matrix in vacuum with $\alpha, \beta = e, \mu, \tau$, $i = 1, 2, 3$ [25]. At present, the constraint on the FTM from the measured flavor ratio is loose. So this minimal theoretical scenario works well. However, precise measurements of the flavor ratio would be available in the near future. Therefore, a more realistic scenario which includes the matter effects or new physics effects should be considered. Various FTMs based on new physics have been proposed, see [26–47] for example. These new physics effects could be tested by the IceCube observatory and the next-generation neutrino telescopes. In this paper, we are concerned about impacts of the matter effects on the flavor transition of HANs. In general, the matter effects arise from the coherent forward elastic and incoherent scattering of HANs with the medium particles. The former affects the flavor conversion through the neutrino mixing matrix in matter. The latter changes not only the flavor composition but also the energy spectrum of HANs. So it might play an important role in the recombination process of HANs in the dense medium[48]. We focus on the matter effects from the elastic scattering in this paper. Particularly, we study the case that the HANs

propagate in gas with a moderate parameter setup. Considering the energy of HANs, the size of the medium, and the profile of the electron density, the FTMs are dependent on the decoherence schemes of neutrinos in the propagation. Even for the same medium, different schemes might lead to different FTMs[49, 50]. In order to understand the matter effects on the flavor transition of HANs comprehensively, we consider five typical types of decoherence schemes in this paper. On the basis of the specific parameters of HANs and the medium, the predictions from these schemes are compared.

The paper is organised as follows. In Sec. II, we describe the mixing matrix and oscillation probability of neutrino in matter. Besides, the FTMs are given on the basis of the decoherence schemes in Refs.[49–52] and the modified version. In Sec. III, a cleaner set of data sample is obtained by constraining the energy of HANs and event topology. Furthermore, we perform a binned maximum likelihood analysis to estimate the electron density in the neutrino propagation path. In Sec. IV, the predictions on the flavor ratio of HANs at Earth from special sources are examined with these FTMs. Identifications of the matter effects are discussed. Finally, we conclude.

II. FTMS BASED ON DIFFERENT DECOHERENCE SCHEMES.

A. The mixing matrix and oscillation probabilities of neutrinos in matter.

In the standard three flavor framework, the effective Hamiltonian H^m in the flavor basis responsible for the propagation of neutrinos in matter can be expressed as[53, 54]

$$H^m = \frac{1}{2E} U \begin{pmatrix} 0 & 0 & 0 \\ 0 & \Delta m_{21}^2 & 0 \\ 0 & 0 & \Delta m_{31}^2 \end{pmatrix} U^\dagger \pm \sqrt{2} G_F \begin{pmatrix} N_e & 0 & 0 \\ 0 & 0 & 0 \\ 0 & 0 & 0 \end{pmatrix} = U^m \begin{pmatrix} E_1 & 0 & 0 \\ 0 & E_2 & 0 \\ 0 & 0 & E_3 \end{pmatrix} U^{m\dagger}. \quad (2)$$

Where E is the neutrino energy, G_F is the Fermi constant, Δm_{21}^2 and Δm_{31}^2 are the neutrino mass-squared difference, and N_e is the electron density along the neutrino's path. For antineutrinos, all terms should be substituted by their complex conjugates and the sign of N_e is negative.

The leptonic mixing matrix in matter, U^m , can be obtained by the diagonalization of H^m . The eigenvalues of H^m are given as[55]

$$E_i = -2\sqrt{Q} \cos\left(\frac{\theta_i}{3}\right) - \frac{a}{3}, \quad i = 1, 2, 3. \quad (3)$$

The components are written as follows[55]:

$$Q = \frac{a^2 - 3b}{9}, \quad (4)$$

$$\theta_1 = \arccos(RQ^{-\frac{3}{2}}), \quad \theta_2 = \theta_1 + 2\pi, \quad \theta_3 = \theta_1 - 2\pi, \quad (5)$$

$$a = -\text{Tr}(H^m), \quad b = \frac{\text{Tr}(H^m)^2 - \text{Tr}(H^{m^2})}{2}, \quad c = \det(H^m), \quad (6)$$

$$R = \frac{2a^3 - 9ab + 27}{54}, \quad (7)$$

where the notations Tr and det represent the trace and determinant, respectively. Accordingly, the elements of U^m are written as follows[55]:

$$U_{ei}^m = \frac{B_i^* C_i}{N_i}, \quad U_{\mu i}^m = \frac{A_i C_i}{N_i}, \quad U_{\tau i}^m = \frac{A_i B_i}{N_i}, \quad (8)$$

where

$$A_i = H_{\mu\tau}(H_{ee} - E_i) - H_{\mu e} H_{e\tau}, \quad (9)$$

$$B_i = H_{\tau e}(H_{\mu\mu} - E_i) - H_{\tau\mu} H_{\mu e}, \quad (10)$$

$$C_i = H_{\mu e}(H_{\tau\tau} - E_i) - H_{\mu\tau} H_{\tau e}, \quad (11)$$

$$N_i^2 = |A_i B_i|^2 + |A_i C_i|^2 + |B_i C_i|^2. \quad (12)$$

The oscillation probabilities can be obtained from[55],

$$P_{\alpha\beta}^m = \delta_{\alpha\beta} - 4 \sum_{j>i} \text{Re}(U_{\beta j}^m U_{\beta i}^{m*} U_{\alpha j}^{m*} U_{\alpha i}^m) \sin^2\left(\frac{L\Delta E_{ji}}{2}\right) + 2 \sum_{j>i} \text{Im}(U_{\beta j}^m U_{\beta i}^{m*} U_{\alpha j}^{m*} U_{\alpha i}^m) \sin(L\Delta E_{ji}), \quad (13)$$

where $\Delta E_{ji} = E_j - E_i$ are the differences between the eigenvalues.

B. FTMs based on different decoherence schemes.

In this section, we introduce five FTMs on the basis of the decoherence schemes of HANs in the propagation. These schemes could be viewed as the boundary conditions in the propagation problem of HANs. First we consider the case that the electron density in the medium varies slowly

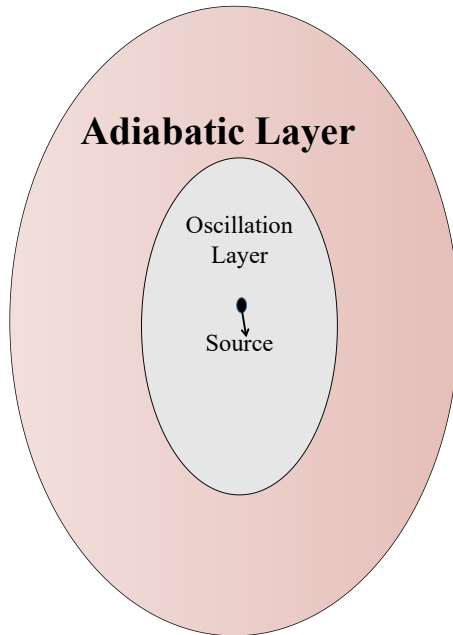


FIG. 1. The schematic figure for the propagation Scheme II in matter.

and the flavor transition of HANs is adiabatic. If the propagation distance in the medium is large enough, the oscillation effects can be neglected. Then we can obtain a simple FTM of the form[52]

$$\bar{P}_{\alpha\beta}^I = \sum_i |U_{\alpha i}^m|^2 |U_{\beta i}|^2, \quad (14)$$

where U^m is the leptonic mixing matrix in matter. In this propagation scheme, there is a decoherence process that changes the flavor state of neutrinos to the eigenstate of the Hamiltonian in matter. Furthermore, in the interface of matter and vacuum the eigenstate of the Hamiltonian in matter correspondingly changes into that in vacuum.

In the case that the oscillation effects should be considered, the adiabatic FTM could be modified as follows

$$\bar{P}_{\alpha\beta}^{II} = \sum_{\gamma} P_{\alpha\gamma}^m \bar{P}_{\gamma\beta}^I, \quad (15)$$

where $P_{\alpha\gamma}^m$ is the neutrino oscillation probability in matter. This FTM shows the process that the flavor of HANs in matter first oscillates and then changes adiabatically, see Fig.1. Furthermore, the decoherence of neutrinos takes place twice in the propagation path. In detail, after the first

decoherence, the superposition of the oscillation amplitude $A_{\alpha\gamma}^m$ is lost. After the second decoherence, that of $U_{\alpha i}^m$ is lost. This decoherence scheme is the adiabatic version of the one introduced in Ref.[49], where the FTM is written as

$$\bar{P}_{\alpha\beta}^{III} = \sum_{\gamma} P_{\alpha\gamma}^m \bar{P}_{\gamma\beta}^S. \quad (16)$$

Note that $\bar{P}_{\gamma\beta}^S$ is the standard FTM shown in Eq.1. In contrast, the flavor state in Scheme III changes into the mass eigenstate in vacuum after the second decoherence.

Another scheme including the oscillation effects can be obtained from the modification of the Scheme III. The corresponding FTM is expressed as [50]

$$\bar{P}_{\alpha\beta}^{IV} = \sum_i \left| \sum_{\gamma} A_{\alpha\gamma}^m U_{\gamma i} \right|^2 |U_{\beta i}|^2. \quad (17)$$

In comparison with $\bar{P}_{\alpha\beta}^{III}$, which can be rewritten as

$$\bar{P}_{\alpha\beta}^{III} = \sum_i \sum_{\gamma} |A_{\alpha\gamma}^m|^2 |U_{\gamma i}|^2 |U_{\beta i}|^2, \quad (18)$$

there is a superposition of the oscillation amplitude in $\bar{P}_{\alpha\beta}^{IV}$. Hence, there is only one decoherence in the propagation which changes the flavor state into the mass eigenstate.

Let us introduce the fifth decoherence scheme which is applied in the case that the electron density is constant. The decoherence is obtained by the integral of the oscillation probability over the whole propagation path, i.e.[51],

$$\bar{P}_{\alpha\beta}^V = \int_0^{L_{vac}} \int_0^L P_{\alpha\beta}(l_{vac}, l_m) dl_{vac} dl_m L_{vac}^{-1} L^{-1}, \quad (19)$$

with

$$\begin{aligned} P_{\alpha\beta}(l_{vac}, l_m) &= |\langle \nu_{\beta} | U e^{-iH_{vac} l_{vac}} U^+ U^m e^{-iH_m l_m} U^{m+} | \nu_{\alpha} \rangle|^2 \\ &= \left| \sum_{\gamma} \sum_i \sum_j U_{\beta i} e^{-iE_i l_{vac}} U_{\gamma i}^* U_{\gamma j}^m e^{-iE_j^m l_m} U_{\alpha j}^{m*} \right|^2 \\ &= \sum_{\gamma} \sum_{\gamma'} \sum_i \sum_{i'} \sum_j \sum_{j'} U_{\beta i} U_{\beta i'}^* e^{-i(E_i - E_{i'}) l_{vac}} U_{\gamma i}^* U_{\gamma' i'} U_{\gamma j}^m U_{\gamma' j'}^{m*} e^{-i(E_j^m - E_{j'}^m) l_m} U_{\alpha j}^{m*} U_{\alpha j'}^m, \end{aligned} \quad (20)$$

where L (L_{vac}) is the propagation distance in matter (vacuum), H_m (H_{vac}) is the diagonal neutrino Hamiltonian matrix in matter (vacuum). When the distance is much larger than the corresponding oscillation length, i.e., $L \gg L^{osc}$, $L_{vac} \gg L_{vac}^{osc}$, the oscillation terms disappear and the averaged oscillation probability can be written as follows

$$\bar{P}_{\alpha\beta}^V = \sum_i \sum_j |U_{\alpha j}^m|^2 P_{ji} |U_{\beta i}|^2 \quad (21)$$

TABLE I. Characteristics of the decoherence schemes

Decoherence Scheme	I	II	III	IV	V
Including adiabatic evolution	yes	yes	no	no	no
Including oscillation effects	no	yes	yes	yes	no
Times of decoherence in the propagation	one	two	two	one	two

with

$$P_{ji} = \left| \sum_{\gamma} U_{\gamma i}^* U_{\gamma j}^m \right|^2. \quad (22)$$

In contrast to Scheme I, besides the first decoherence that changes the flavor state to the eigenstate of the Hamiltonian in matter, there is another decoherence that changes the eigenstate of the Hamiltonian in matter into that in vacuum, i.e., $|\nu_j\rangle^m \rightarrow |\nu_i\rangle$.

Now we have introduced five typical decoherence schemes for the propagation problem of HANs in matter. For the sake of inter-comparison, their characteristics are listed in Tab.I. In the following sections, we shall estimate the the electron density in the propagation path of HANs and examine the predictions from the decoherence schemes with specific parameters of HANs and matter.

III. LIKELIHOOD ANALYSIS ON THE ELECTRON DENSITY

In this section, we give an simplified estimate for the electron density in the propagation path of HANs with the high-energy starting events (HESE) detected by the IceCube observatory.

A. Data Sample

The analyses performed in this article utilize the full 2078-day HESE sample that contains 82 events[2, 56, 57]. The event number 32 and event number 55 were produced by a coincident pair of background muons from unrelated cosmic ray air showers and are excluded from the analysis. The remaining events possess complete information that is associated with event topology (showers or tracks) and neutrino arrival direction (up-going or down-going). Here, showers are produced by the charged-current(CC) neutrino-nucleon scattering of $\nu_e(\bar{\nu}_e)$ or $\nu_{\tau}(\bar{\nu}_{\tau})$ and the neutral current(NC) interactions from all flavors in the ice around the detectors[1–5]. Tracks are generated by the CC deep inelastic scattering of $\nu_{\mu}(\bar{\nu}_{\mu})$ [1–5]. Given the small amount of data in this sample, we need

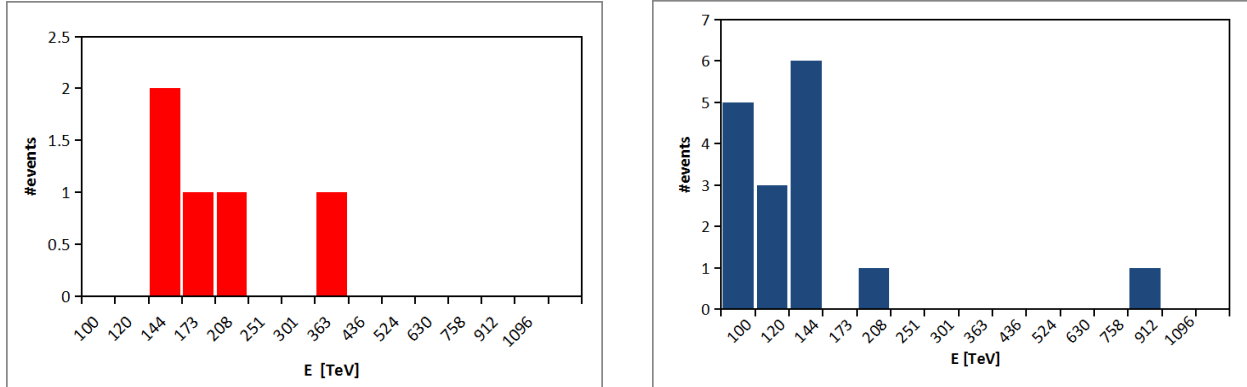


FIG. 2. The energy distribution of up- and down-going shower events in the energy range 100TeV-1PeV. Left panel: up-going shower events, Right panel: down-going shower events.

a cleaner events set to obtain reliable analysis results[9]. Based on this point, we set an energy range: 100TeV-1PeV, which eliminates the background induced by atmospheric muons, atmospheric neutrinos and prompt neutrinos[4, 58, 59].

Furthermore, we consider the case that some fraction of the tracks could be misidentified as showers. The reason is that a muon neutrino produces a muon near the edge of the detector. In addition, in the SM, the ratio of NC to CC showers at a fixed energy, is smaller than 0.04[9]. To sum up, we focus on the shower events with CC interaction in this paper and the energy range 100TeV-1PeV. Accordingly, we consider 21 events: 5 events come from the northern hemisphere and 16 events from the southern hemisphere. The energy distribution of these events are shown in Fig.2.

B. Maximum Likelihood Analysis

On the basis of the above setting of HAN events, we estimate the electron density(N_e) along the neutrino propagation path, using a binned maximum likelihood method. The expected number of events per bin k is given by[9]

$$N_k^x(N_e) = 2\pi T \left(\int_k \Phi_{\nu_e + \bar{\nu}_e}^x(E, N_e) A_{e,k}^x(E) dE + \int_k \Phi_{\nu_\tau + \bar{\nu}_\tau}^x(E, N_e) A_{\tau,k}^x(E) dE \right), \quad (23)$$

where $x \in \{u, d\}$, is hemispherical direction, $T=2078$ days is the time of data taking, and \int_k represents the integration along that bin. $A_{\alpha,k}^x(E)$, $\alpha \in \{e, \tau\}$, is the effective area in the k -th energy bin, which has been published by the IceCube Collaboration[60] and is shown in Fig.3. Here $\Phi_{\nu_\alpha + \bar{\nu}_\alpha}^x(E, N_e)$ is the diffuse flux of $\nu_\alpha + \bar{\nu}_\alpha$ with hemispherical direction $x \in \{u, d\}$, which is

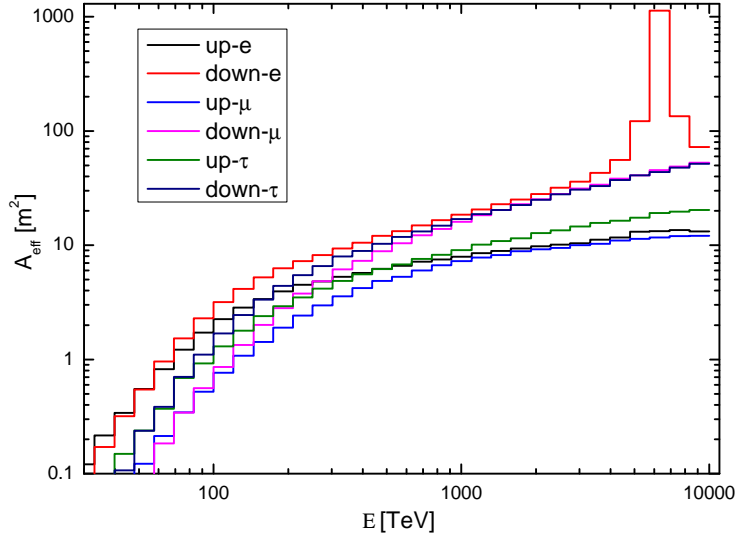


FIG. 3. IceCube effective areas for the different neutrino species[60].

TABLE II. The best fit values and 68% confidence level of energy-spectrum parameters of HANs for the North-South Model[61].

Parameters	Best fit	68% C.L.
ϕ_u	2.1	0.5 - 5.0
γ_u	2.0	1.6 - 2.3
ϕ_d	6.8	5.3 - 8.4
γ_d	2.56	2.44 - 2.67

written as

$$\Phi_{\nu_{\alpha}+\bar{\nu}_{\alpha}}^x(E, N_e) = \phi_x \left(\frac{E}{100 \text{ TeV}} \right)^{-\gamma_x} \cdot \left(\sum_{\beta=e,\mu,\tau} \bar{P}_{\alpha\beta}(E, N_e) \Phi_{\beta}^S \right) \cdot 10^{-18} \text{ GeV}^{-1} \text{ cm}^{-2} \text{ s}^{-1} \text{ sr}^{-1}. \quad (24)$$

The ranges of the normalization ϕ_x and the spectral index γ_x at the 68% confidence level are listed in Tab.II. $\bar{P}_{\alpha\beta}(E, N_e) \in \{\bar{P}_{\alpha\beta}^I, \bar{P}_{\alpha\beta}^V\}$ is the flavor transition matrix. Because the flavor ratio of HANs at the source is uncertain at present, we set a general original flavor composition $\Phi_{\beta}^S = (y, 1-y, 0)^T$, with random values in the range $0 \leq y \leq 1$. Let \bar{N}_k^x be the measured number of events with hemispherical direction $x \in \{u, d\}$ in the energy bin k , which are shown in Fig.2. In

TABLE III. The most likely ranges of electron density N_e from the Fig.4.

Decoherence Scheme	Hemispherical Direction	The most likely ranges of N_e cm ⁻³
I	up-going	$[5.5 \times 10^{18}, 6.5 \times 10^{18}]$
I	down-going	$[8.0 \times 10^{17}, 1.0 \times 10^{18}]$ or $[4.5 \times 10^{19}, 5.5 \times 10^{19}]$
V	up-going	$[1.6 \times 10^{18}, 1.7 \times 10^{18}]$ or $[1.3 \times 10^{19}, 1.4 \times 10^{19}]$
V	down-going	$[2.2 \times 10^{18}, 2.7 \times 10^{18}]$ or $[2.5 \times 10^{19}, 2.6 \times 10^{19}]$

the meantime, we assume that the expected number $N_k^x(N_e)$ is given by a poisson distribution

$$P[\overline{N}_k^x | N_k^x(N_e)] = \frac{N_k^x(N_e)^{\overline{N}_k^x}}{\overline{N}_k^x!} \exp\{-N_k^x(N_e)\}. \quad (25)$$

The likelihood for each hemispherical direction $x \in \{u, d\}$ is

$$L(N_e) = \prod_k P[\overline{N}_k^x | N_k^x(N_e)]. \quad (26)$$

Taking the logarithm of both sides of Eq.26, we obtain the following expression,

$$\ln[L(N_e)] = \sum_k \ln\{ P[\overline{N}_k^x | N_k^x(N_e)] \}. \quad (27)$$

Now we sample randomly from the 3σ level with the normal mass ordering of $\sin^2 \theta_{12}$, $\sin^2 \theta_{13}$, $\sin^2 \theta_{23}$, δ_{CP} , Δm_{21}^2 and Δm_{31}^2 , which have been published in the global analysis NuFit 5.0[62]. Analogously, we sample randomly from the 68% confidence level of energy-spectrum parameters of HANs for the North-South Model listed in Tab.II. Substituting these parameters value into Eq.28, a set of likelihood functions, $\ln[L(N_e)]$, could be obtained(see Fig.4).

Here we show the likelihood function with the typical adiabatic Scheme I and the non-adiabatic Scheme V. For the both schemes, we can see that the curves from up-going direction are smooth relative to one from down-going direction. The reason is that the number of statistics from up-going direction is less than one from down-going direction. Fig.4 also shows that the matter effect is negligible when $N_e < 10^{17} \text{cm}^{-3}$ and the variation of $-\ln[L(N_e)]$ is moderate in the N_e range $[10^{16}, 10^{20}] \text{cm}^{-3}$. Thus, the HESEs bring no strong constraints on the electron density in gas which is a realistic environment for the promising source of HANs. In the following section, we will examine the impacts of N_e on the flavor ratio at Earth in the N_e range $[10^{17}, 10^{19}] \text{cm}^{-3}$. Specifically, we focus on the most likely ranges of electron density N_e from the Fig.4, which is listed in Tab.III. For Scheme I, we pay attention to the ranges of electron density: $[8.0 \times 10^{17}, 1.0 \times 10^{18}] \text{cm}^{-3}$, $[5.5 \times 10^{18}, 6.5 \times 10^{18}] \text{cm}^{-3}$ and $[4.5 \times 10^{19}, 5.5 \times 10^{19}] \text{cm}^{-3}$. For Scheme V, we concern the ranges of electron density: $[1.6 \times 10^{18}, 2.7 \times 10^{18}] \text{cm}^{-3}$ and $[1.3 \times 10^{19}, 2.6 \times 10^{19}] \text{cm}^{-3}$.

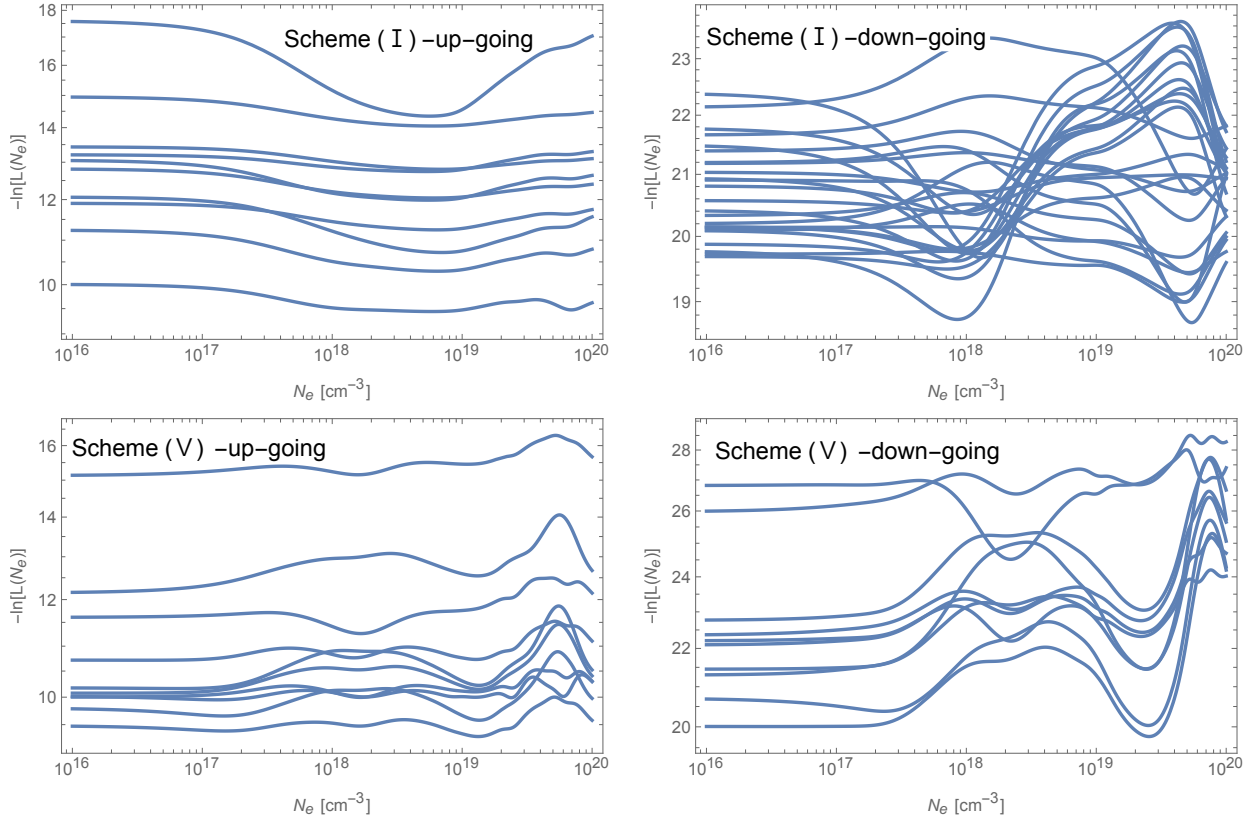


FIG. 4. The relation between the likelihood function $-\ln[L(N_e)]$ and electron density N_e with the given hemispherical direction for Scheme I and Scheme V.

TABLE IV. Parameters of neutrinos and matter for the propagation schemes

Scheme	Distance in vacuum (L_{vac})	Distance in matter(L)	Neutrino energy (E)
II, III, IV	$\gg L_{vac}^{osc}$	$[10^5, 10^8]\text{km}$	$[10^2, 10^3]\text{TeV}$
I, V	$\gg L_{vac}^{osc}$	$\gg L^{osc}$	$[10^2, 10^3]\text{TeV}$

IV. PREDICTIONS ON THE FLAVOR RATIO INCLUDING MATTER EFFECTS

In this section we examine the predicted flavor ratio at Earth from the given FTMs. The specific parameters of the HANs and matter for the corresponding propagation scheme are listed in Tab.IV. In the meantime, we assuming that the range of the electron density N_e for Scheme II is identical to the one for Scheme I and N_e for Scheme III and Scheme IV is equal to that for Scheme V.

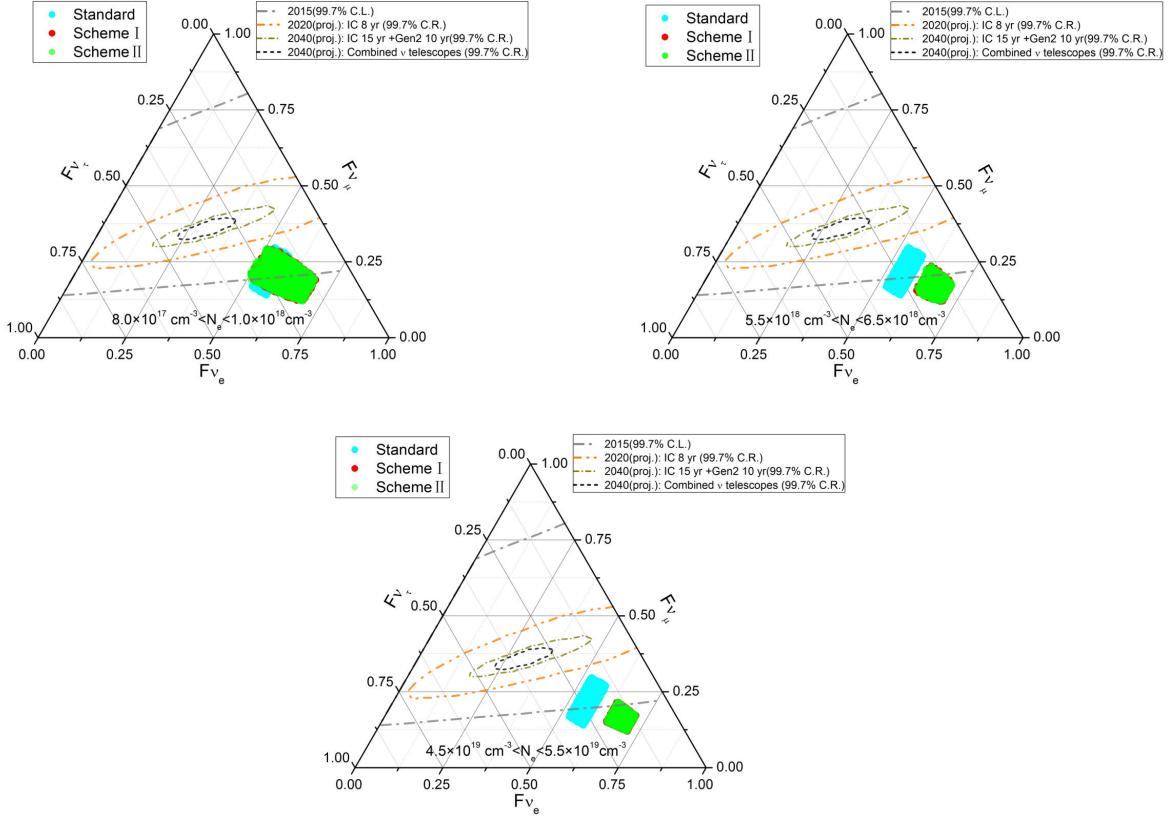


FIG. 5. Ternary plot of the flavor ratio at Earth with the neutron-decay source on the basis of the global fit data at 3σ level[62] with the normal mass ordering and the parameters in Tab.III and Tab.IV. Their FTMs include adiabatic evolution. The 2015 3σ constraint is taken from Ref.[61]. The 2020 and 2040 3σ credible regions with the pion-decay source based on IceCube and IceCube-Gen2 are taken from Ref.[21]. The 3σ credible region with the pion-decay source based on all TeV-PeV neutrino telescopes available in 2040 is taken from Ref.[15].

We consider three typical sources, i.e.,

$$\begin{aligned}
 & \text{neutron - decay source with } \Phi^s = (1, 0, 0), \\
 & \text{pion - decay source with } \Phi^s = (1/3, 2/3, 0), \\
 & \text{muon - damping source with } \Phi^s = (0, 1, 0),
 \end{aligned} \tag{28}$$

where Φ^s is the flavor ratio at the source. Using Φ^s and the aforementioned FTMs, we can obtain the flavor ratio of HANs at Earth. On the bases of the given parameters in Tab.IV, and the recent global fit data of neutrinos oscillations[62], the ternary plots for the flavor ratio are shown in Fig.5-Fig.10. For the sake of comparison, the flavor ratio predicted by the standard scheme is also shown in these figures. From the figures, we can obtain the following observations.

For the neutron-decay source (see Fig.5 and Fig.6), the predicted flavor ratio from the FTMs

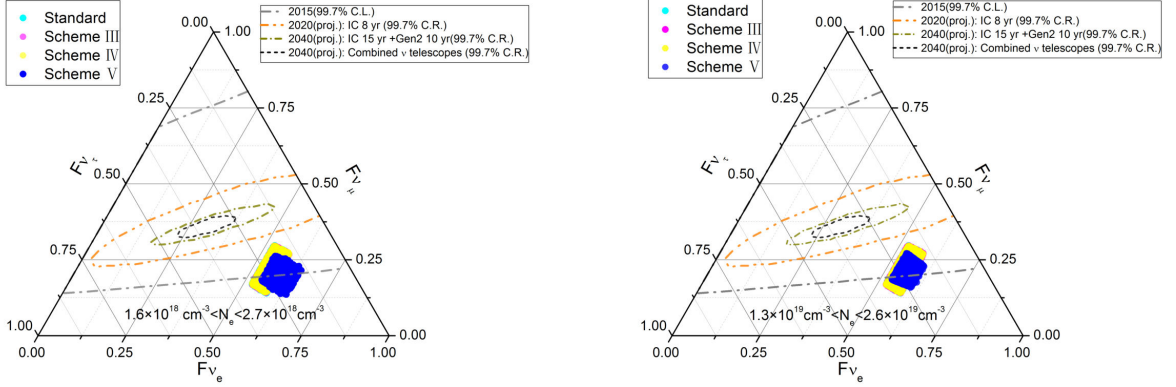


FIG. 6. Ternary plot of the flavor ratio at Earth with the neutron-decay source. Their FTMs exclude adiabatic evolution. The conventions of parameters are the same as those in Fig.5.

can be classified into three regions as follows. (a). The red region from Scheme I: It is the same as the green one from Scheme II, which can enlarge the region of the flavor ratio at Earth with $N_e \in [8.0 \times 10^{17}, 1.0 \times 10^{18}] \text{ cm}^{-3}$. Whereas for $N_e \in [5.5 \times 10^{18}, 6.5 \times 10^{18}] \text{ cm}^{-3}$ or $N_e \in [4.5 \times 10^{19}, 5.5 \times 10^{19}] \text{ cm}^{-3}$, the region from Scheme I or II is completely different from the one predicted from the standard scheme. (b). The magenta region from Scheme III: It is identical to the yellow one from Scheme IV or the cyan region from the standard scheme. (c). The blue region from Scheme V: There is a significant contraction and moderate deviation of the region of the flavor ratio, with respect to one from the standard scheme. However, all the predicted regions are at the margin of the 2015 ICECube 3σ constraint[62]. Considering the 2040 expected sensitivity on the flavor ratio[15, 21], these regions may be precluded by the observations of the neutrino telescopes in the near future.

For the muon-damping source (see Fig.7 and Fig.8), the predicted flavor ratio could also be classified into three regions as follows. (a). The red region from Scheme I: Since the oscillation effect is not notable for Scheme II, this region is nearly identical to that from Scheme II. We note that, for $N_e \in [5.5 \times 10^{18}, 6.5 \times 10^{18}] \text{ cm}^{-3}$, the predicted region from the Scheme I or II does not overlap with the one from the standard scheme (see Fig.7). (b). The magenta region from Scheme III: It is identical to the yellow one from Scheme IV or the cyan region from the standard scheme. (c). The blue region from Scheme V: the predicted region both pass through the 2040 3σ credible region [15]. Therefore, it is a promising source of HANs.

For the pion-decay source (see Fig.9 and Fig.10), the predicted flavor ratio could be classified into three regions as follows. (a). The region from Scheme I: Since the oscillation effect is not

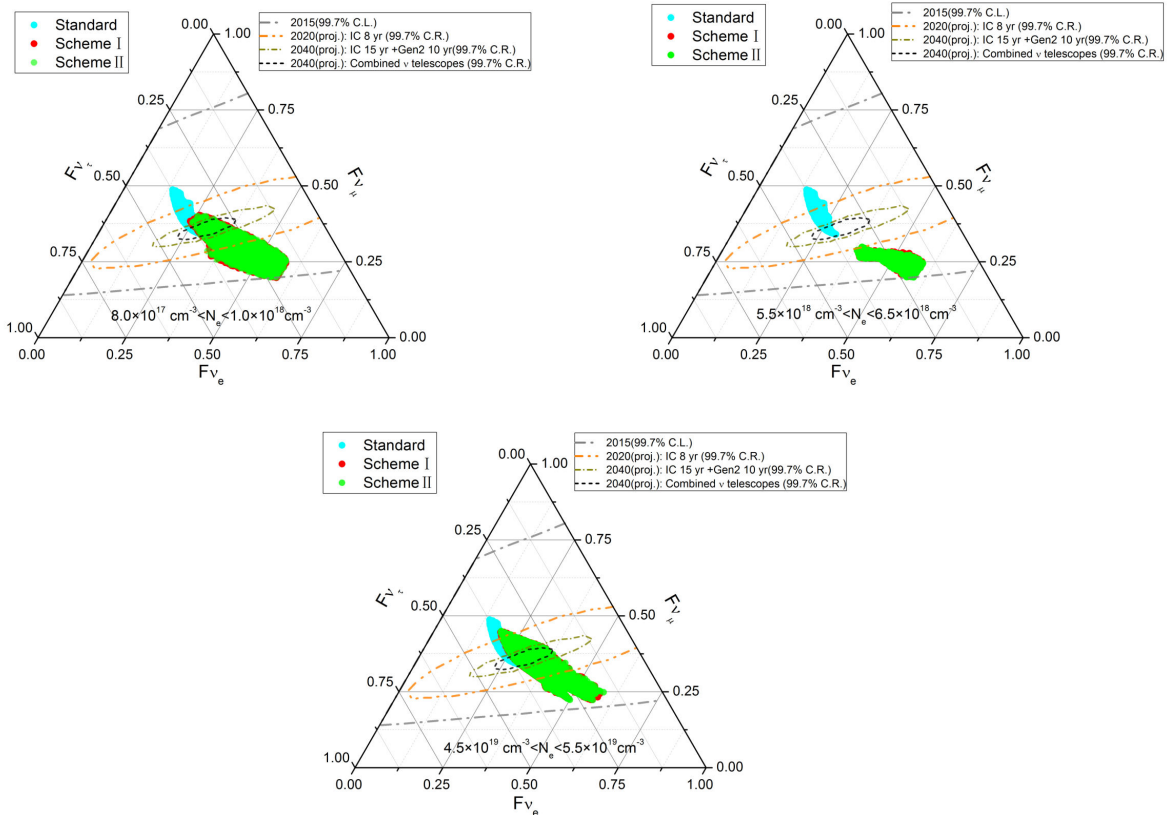


FIG. 7. Ternary plot of the flavor ratio at Earth with the muon-damping source. Their FTMs include adiabatic evolution. The conventions of parameters are the same as those in Fig.5.

notable for Scheme II, this region is nearly identical to that from Scheme II. Nearly half of the area overlaps with the 2040 3σ credible region [15] with different electron density intervals. So Scheme I and II might work in the era of precise measurement of the flavor ratio. In the range $N_e \in [5.5 \times 10^{18}, 6.5 \times 10^{18}] \text{cm}^{-3}$, the predicted region from the Scheme I or II does not overlap with the one from the standard scheme (see Fig.7). (b). The magenta region from Scheme III: It is identical to the yellow one from Scheme IV or the cyan region from the standard scheme. Meanwhile, the blue region from Scheme V has a moderate deviation with respect to the one from the standard scheme. Nearly half of the areas overlaps the 3σ credible region [15].

On the bases of the above observations from the figures, we can obtain the following conclusions:

- The predicted regions of the flavor ratio at Earth can be classified into 4 types, irrespective of the production sources. They are the region from the standard scheme, the one from the Scheme I or II, the one from the Scheme III or IV, and the one from Scheme V, respectively.
- The identification of the matter effect on the flavor ratio is difficult in general. The most

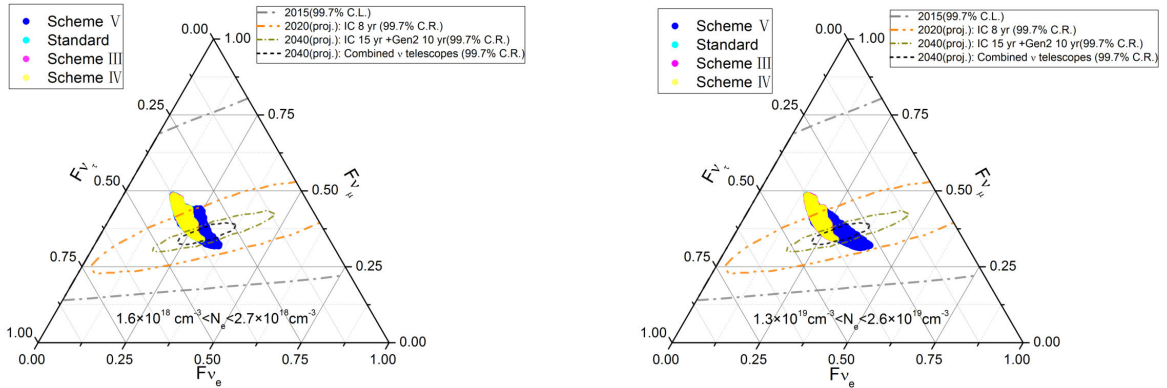


FIG. 8. Ternary plot of the flavor ratio at Earth with the muon-damping source. Their FTMs exclude adiabatic evolution. The conventions of parameters are the same as those in Fig.5.

notable effect take places when the FTM is from the adiabatic schemes, namely the Scheme I and II. In the range $N_e \in [5.5 \times 10^{18}, 6.5 \times 10^{18}] \text{cm}^{-3}$, the region of the flavor ratio from the adiabatic schemes is completely different from the one from the standard scheme, irrespective of the production sources.

V. CONCLUSIONS

A precise measurement of the flavor ratio of HANs may be available in the near future. To test the matter effects on the flavor transition of HANs by the next-generation neutrino telescopes deserves considerations. The matter effects are dependent on the propagation scheme of the HANs and the production sources. We introduced five typical decoherence schemes for the propagation of HANs. On the basis of the data of HNSE from IceCube, the electron density N_e was estimated with a likelihood analysis. By now, the constrains from HNSEs on N_e is weak. Thus, a wide range of N_e can be taken into account for the gas environment of HANs. Accordingly, the matter effects on the flavor ratio at Earth were examined for the typical sources and the likely range of N_e . In general, the predicted region of the flavor ratio including the matter effect overlaps with the one from the standard scheme. However, for the adiabatic schemes I, II, the identification of the matter effects in the special range of the electron density is promising, irrespective of the production sources of HANs. Therefore, constraints on the matter parameters and propagation path might be deduced from the measured flavor ratio in the near future.

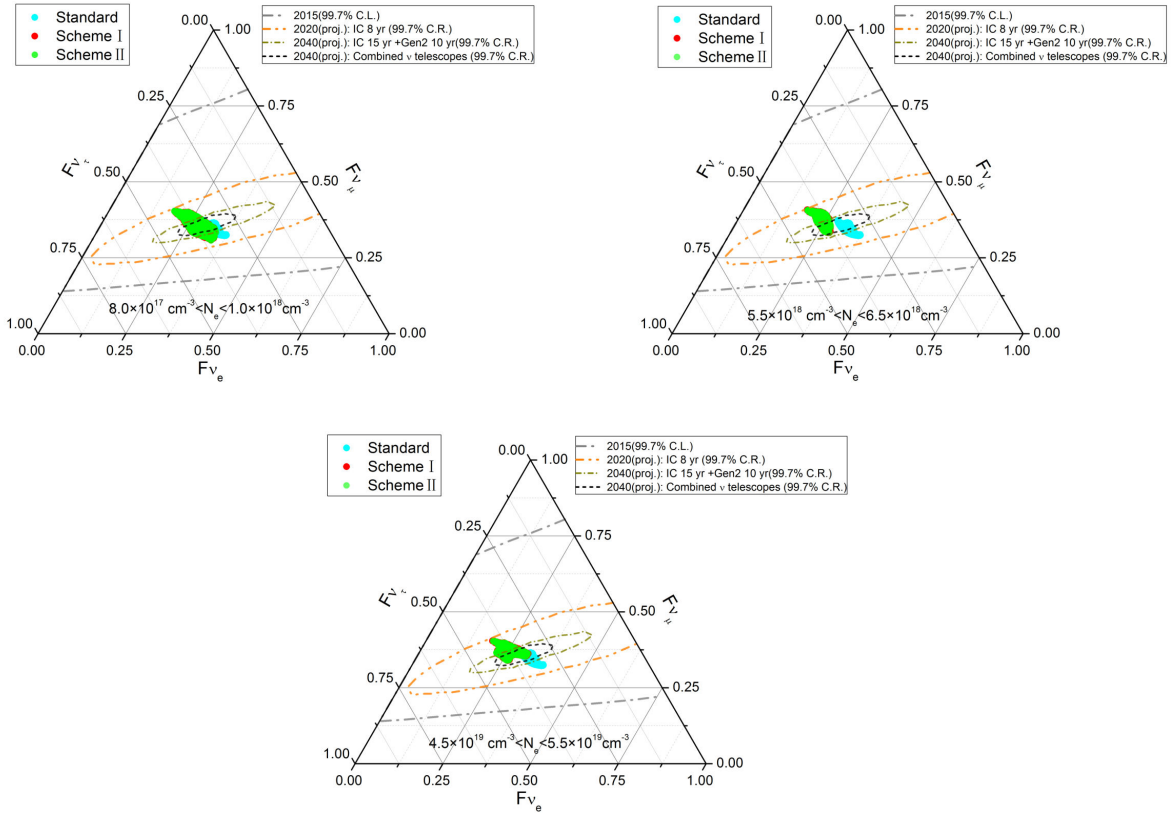


FIG. 9. Ternary plot of the flavor ratio at Earth with the pion-decay source. Their FTMs include adiabatic evolution. The conventions of parameters are the same as those in Fig.5.

ACKNOWLEDGMENTS

This work is supported by the National Natural Science Foundation of China under grant No. 12065007, the Guangxi Scientific Programm Foundation under grant No. Guike AD19110045, the Research Foundation of Guilin University of Technology under grant No. GUTQDJJ2018103.

-
- [1] M. G. Aartsen *et al.* (IceCube), Phys. Rev. Lett. **111**, 021103 (2013), arXiv:1304.5356 [astro-ph.HE].
 - [2] M. G. Aartsen *et al.* (IceCube), Phys. Rev. Lett. **113**, 101101 (2014), arXiv:1405.5303 [astro-ph.HE].
 - [3] M. G. Aartsen *et al.* (IceCube), Phys. Rev. Lett. **115**, 081102 (2015), arXiv:1507.04005 [astro-ph.HE].
 - [4] M. G. Aartsen *et al.* (IceCube), Astrophys. J. **833**, 3 (2016), arXiv:1607.08006 [astro-ph.HE].
 - [5] M. G. Aartsen *et al.* (IceCube), Nature **591**, 220 (2021), [Erratum: Nature 592, E11 (2021)], arXiv:2110.15051 [hep-ex].

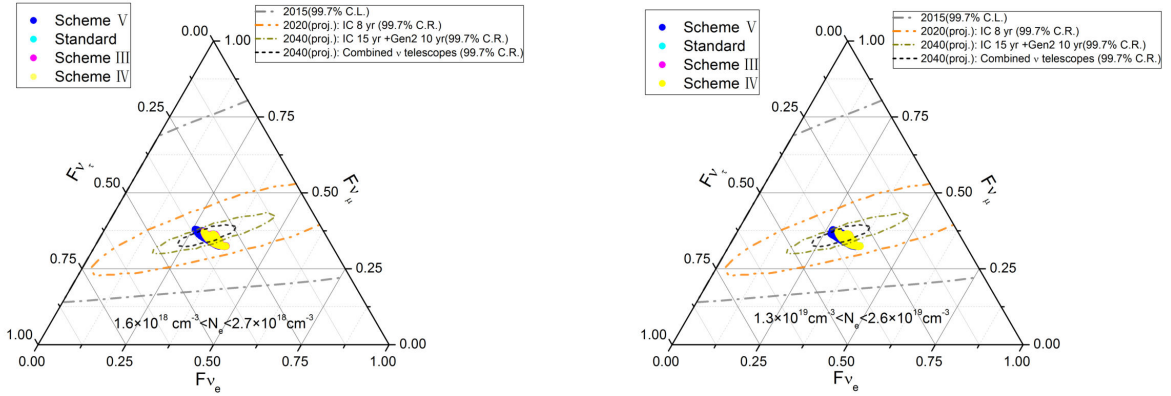


FIG. 10. Ternary plot of the flavor ratio at Earth with the pion-decay source. Their FTMs exclude adiabatic evolution. The conventions of parameters are the same as those in Fig.5.

- [6] A. Watanabe, JCAP **08**, 030 (2015), arXiv:1412.8264 [astro-ph.HE].
- [7] C.-Y. Chen, P. S. Bhupal Dev, and A. Soni, Phys. Rev. D **92**, 073001 (2015), arXiv:1411.5658 [hep-ph].
- [8] S. Palomares-Ruiz, A. C. Vincent, and O. Mena, Phys. Rev. D **91**, 103008 (2015), arXiv:1502.02649 [astro-ph.HE].
- [9] L. A. Anchordoqui, M. M. Block, L. Durand, P. Ha, J. F. Soriano, and T. J. Weiler, Phys. Rev. D **95**, 083009 (2017), arXiv:1611.07905 [astro-ph.HE].
- [10] R. Abbasi *et al.* (IceCube), Phys. Rev. D **104**, 022002 (2021), arXiv:2011.03545 [astro-ph.HE].
- [11] M. G. Aartsen *et al.* (IceCube, Fermi-LAT, MAGIC, AGILE, ASAS-SN, HAWC, H.E.S.S., INTEGRAL, Kanata, Kiso, Kapteyn, Liverpool Telescope, Subaru, Swift NuSTAR, VERITAS, VLA/17B-403), Science **361**, eaat1378 (2018), arXiv:1807.08816 [astro-ph.HE].
- [12] M. G. Aartsen *et al.* (IceCube), Science **361**, 147 (2018), arXiv:1807.08794 [astro-ph.HE].
- [13] R. Stein *et al.*, Nature Astron. **5**, 510 (2021), arXiv:2005.05340 [astro-ph.HE].
- [14] Y. Cendes, K. D. Alexander, E. Berger, T. Eftekhari, P. K. G. Williams, and R. Chornock, Astrophys. J. **919**, 127 (2021), arXiv:2103.06299 [astro-ph.HE].
- [15] N. Song, S. W. Li, C. A. Argüelles, M. Bustamante, and A. C. Vincent, JCAP **04**, 054 (2021), arXiv:2012.12893 [hep-ph].
- [16] R. Abbasi *et al.* (IceCube), (2020), arXiv:2011.03561 [hep-ex].
- [17] X. Rodrigues, S. Gao, A. Fedynitch, A. Palladino, and W. Winter, Astrophys. J. Lett. **874**, L29 (2019), arXiv:1812.05939 [astro-ph.HE].
- [18] R. Xue, R.-Y. Liu, M. Petropoulou, F. Oikonomou, Z.-R. Wang, K. Wang, and X.-Y. Wang, Astrophys. J. **886**, 23 (2019), arXiv:1908.10190 [astro-ph.HE].
- [19] K. Murase and F. W. Stecker, (2022), arXiv:2202.03381 [astro-ph.HE].
- [20] A. A. D. *et al.* (Baikal-GVD), PoS **ICHEP2020**, 606 (2021), arXiv:2012.03373 [astro-ph.HE].
- [21] M. G. Aartsen *et al.* (IceCube-Gen2), J. Phys. G **48**, 060501 (2021), arXiv:2008.04323 [astro-ph.HE].

- [22] S. Adrian-Martinez *et al.* (KM3Net), *J. Phys. G* **43**, 084001 (2016), arXiv:1601.07459 [astro-ph.IM].
- [23] M. Agostini *et al.* (P-ONE), *Nature Astron.* **4**, 913 (2020), arXiv:2005.09493 [astro-ph.HE].
- [24] A. Romero-Wolf *et al.*, in *Latin American Strategy Forum for Research Infrastructure* (2020) arXiv:2002.06475 [astro-ph.IM].
- [25] J. Beringer *et al.* (Particle Data Group), *Phys. Rev. D* **86**, 010001 (2012).
- [26] J. F. Beacom, N. F. Bell, D. Hooper, S. Pakvasa, and T. J. Weiler, *Phys. Rev. Lett.* **90**, 181301 (2003), arXiv:hep-ph/0211305.
- [27] D. Meloni and T. Ohlsson, *Phys. Rev. D* **75**, 125017 (2007), arXiv:hep-ph/0612279.
- [28] C. A. Argüelles, T. Katori, and J. Salvado, *Phys. Rev. Lett.* **115**, 161303 (2015), arXiv:1506.02043 [hep-ph].
- [29] P. Mehta and W. Winter, *JCAP* **03**, 041 (2011), arXiv:1101.2673 [hep-ph].
- [30] K. S. Babu, V. Brdar, A. de Gouvêa, and P. A. N. Machado, (2021), arXiv:2108.11961 [hep-ph].
- [31] P. Baerwald, M. Bustamante, and W. Winter, *JCAP* **10**, 020 (2012), arXiv:1208.4600 [astro-ph.CO].
- [32] G. Pagliaroli, A. Palladino, F. L. Villante, and F. Vissani, *Phys. Rev. D* **92**, 113008 (2015), arXiv:1506.02624 [hep-ph].
- [33] M. Bustamante, J. F. Beacom, and K. Murase, *Phys. Rev. D* **95**, 063013 (2017), arXiv:1610.02096 [astro-ph.HE].
- [34] S. Choubey, S. Goswami, and D. Pramanik, *JHEP* **02**, 055 (2018), arXiv:1705.05820 [hep-ph].
- [35] P. B. Denton and I. Tamborra, *Phys. Rev. Lett.* **121**, 121802 (2018), arXiv:1805.05950 [hep-ph].
- [36] S. Parke and M. Ross-Lonergan, *Phys. Rev. D* **93**, 113009 (2016), arXiv:1508.05095 [hep-ph].
- [37] V. Brdar, J. Kopp, and X.-P. Wang, *JCAP* **01**, 026 (2017), arXiv:1611.04598 [hep-ph].
- [38] J. Tang, Y. Zhang, and Y.-F. Li, *Phys. Lett. B* **774**, 217 (2017), arXiv:1708.04909 [hep-ph].
- [39] C. A. Argüelles, K. Farrag, T. Katori, R. Khandelwal, S. Mandalia, and J. Salvado, *JCAP* **02**, 015 (2020), arXiv:1909.05341 [hep-ph].
- [40] S. A. R. Ellis, K. J. Kelly, and S. W. Li, *JHEP* **12**, 068 (2020), arXiv:2008.01088 [hep-ph].
- [41] M. Kobayashi and C. S. Lim, *Phys. Rev. D* **64**, 013003 (2001), arXiv:hep-ph/0012266.
- [42] J. F. Beacom, N. F. Bell, D. Hooper, J. G. Learned, S. Pakvasa, and T. J. Weiler, *Phys. Rev. Lett.* **92**, 011101 (2004), arXiv:hep-ph/0307151.
- [43] A. Esmaili, *Phys. Rev. D* **81**, 013006 (2010), arXiv:0909.5410 [hep-ph].
- [44] E. W. Kolb and M. S. Turner, *Phys. Rev. D* **36**, 2895 (1987).
- [45] K. Ioka and K. Murase, *PTEP* **2014**, 061E01 (2014), arXiv:1404.2279 [astro-ph.HE].
- [46] M. Bustamante, J. F. Beacom, and W. Winter, *Phys. Rev. Lett.* **115**, 161302 (2015), arXiv:1506.02645 [astro-ph.HE].
- [47] N. Klop and S. Ando, *Phys. Rev. D* **97**, 063006 (2018), arXiv:1712.05413 [hep-ph].
- [48] A. G. Soto, P. Zhelnin, I. Safa, and C. A. Argüelles, *Phys. Rev. Lett.* **128**, 171101 (2022), arXiv:2112.06937 [hep-ph].
- [49] O. Mena, I. Mocioiu, and S. Razzaque, *Phys. Rev. D* **75**, 063003 (2007), arXiv:astro-ph/0612325.

- [50] S. Razzaque and A. Y. Smirnov, *JHEP* **03**, 031 (2010), arXiv:0912.4028 [hep-ph].
- [51] R. W. Rasmussen, L. Lechner, M. Ackermann, M. Kowalski, and W. Winter, *Phys. Rev. D* **96**, 083018 (2017), arXiv:1707.07684 [hep-ph].
- [52] S.-J. Rong and D.-H. Xu, *Adv. High Energy Phys.* **2022**, 6949022 (2022), arXiv:2110.15597 [hep-ph].
- [53] L. Wolfenstein, *Phys. Rev. D* **17**, 2369 (1978).
- [54] S. P. Mikheyev and A. Y. Smirnov, *Sov. J. Nucl. Phys.* **42**, 913 (1985).
- [55] K. Abe *et al.* (Super-Kamiokande), *Phys. Rev. D* **91**, 052003 (2015), arXiv:1410.4267 [hep-ex].
- [56] C. Kopper, W. Giang, and N. Kurahashi (ICECUBE), *PoS ICRC2015*, 1081 (2016).
- [57] C. Kopper (IceCube), *PoS ICRC2017*, 981 (2018).
- [58] F. Halzen and L. Wille, (2016), arXiv:1601.03044 [hep-ph].
- [59] F. Halzen and L. Wille, *Phys. Rev. D* **94**, 014014 (2016), arXiv:1605.01409 [hep-ph].
- [60] M. G. Aartsen *et al.* (IceCube), *Science* **342**, 1242856 (2013), arXiv:1311.5238 [astro-ph.HE].
- [61] M. G. Aartsen *et al.* (IceCube), *Astrophys. J.* **809**, 98 (2015), arXiv:1507.03991 [astro-ph.HE].
- [62] I. Esteban, M. C. Gonzalez-Garcia, M. Maltoni, T. Schwetz, and A. Zhou, *JHEP* **09**, 178 (2020), arXiv:2007.14792 [hep-ph].